https://doi.org/10.1016/j.msea.2015.04.027

ZrCu-based bulk metallic glass composites with large strain-hardening capability

F.F. Wu[a,b*], K.C. Chan[a**], S.H. Chen[a], S.S. Jiang[b], G. Wang[c]

[a]*Advanced Manufacturing Technology Research Centre, Department of Industrial and Systems Engineering, Hong Kong Polytechnic University, Kowloon, Hong Kong, China*

[b]*School of Materials Science and Engineering, Liaoning University of Technology, Jinzhou 121001, China*

[c]*Laboratory for Microstructures, Shanghai University, Shanghai200444, China*

ABSTRACT

A large tensile plastic deformation was reached in ZrCu-based metallic glass composites with metastable B2 phase. It was found that the B2 phase can effectively promote the density of the stress concentration sites and enhance the formation and interaction of multiple shear bands, which significantly stabilize the tensile plastic deformation of metallic glass composites. Based on the concept of the normalized strain-hardening rate, the critical volume fraction for the stable tensile plastic deformation of metallic glass composites was determined.

Keywords: Metallic glass composite; tensile plasticity; plastic deformation; fracture

* Corresponding author: Email: ffwooxy@163.com
** Corresponding author: Email: kc.chan@polyu.edu.hk

1. Introduction

Extensive investigation over the past few years has indicated that the strength of metallic glass (MG) is greatly increased in the absence of dislocation defects. However, the poor tensile ductility of MG is still a key issue to be addressed [1-3]. Though most MGs show brittle fracture behavior macroscopically, it is believed that the shear strain in a single shear band in an MG can be as large as 10^{2-3}, or more [4-6]. Therefore, MG should be intrinsically ductile at the micron scale, a fact that is verified by a number of reports on the mechanical behavior of MG with sizes decreasing to the micrometer or nanometer levels [3,7-10]. Therefore, a crystalline phase can be *ex-situ* or *in-situ* introduced to decrease the effective geometric size of the MG matrix in MG composites (MGCs), thereby inhibiting the unstable and rapid propagation of major shear bands [11-14]. In such MGCs, since multiple shear bands are activated in the MG matrix, the ductility of MGCs is greatly improved, especially in those body-centered cubic (bcc) β dendrite reinforced ZrTi-based MGCs [15-18]. Usually, β dendrite reinforced MGCs show unstable plastic deformation under tension: strong necking or strain localization occurs once they yield [18]. This unstable plastic deformation is attributed to the low work-hardening capability of the β dendrites, which is characterized by a few dislocations with same orientation and no dislocation interaction [18,19]. Therefore, the dendrites are easily cut off by the propagating shear bands in the MG matrix [18]. To overcome this unstable plastic deformation under tension, metastable phases were introduced to the MG matrix, such as metastable β phase reinforced Ti-based MGCs [20] and metastable bcc B2 phased reinforced CuZr-based MGCs [21-25]. These MGCs not only showed excellent compressive properties, but also displayed a strong work-hardening rate under tension. Due to the martensitic transformation of the B2 phase during plastic deformation at room temperature, stress redistribution near the B2/MG interface and transformation mediated plasticity can be observed [21-25].

In this study, the tensile plastic deformation of ZrCu-based MGCs with different volume fractions of the metastable B2 phase was systematically investigated, and a large uniform tensile plasticity was successfully achieved in the ZrCu-based MGCs.

2. Experimental

The ZrCu-based MGs and MGCs with chemical compositions of $Zr_{48}Cu_{46.5}Al_4Nb_{1.5}$ were prepared by arc melting and cast into a copper mold. Ingots with length of 50 mm and diameters of 3 mm, 3.5 mm, and 4 mm were produced. $Zr_{48}Cu_{46.5}Al_4Nb_{1.5}$ MGs with diameters of 3 mm, 3.5 mm, and 4.0 mm were labelled S1, S2, and S3, respectively. The phases of the MG and MGC ingots were characterized by X-ray diffraction (XRD) using a Rigaku diffractometer with Cu K_α radiation. The microstructure was also examined by using a JEM 6490 scanning electronic microscope (SEM) and a Carl Zeiss optical microscope (OM). The volume fraction of the B2 phase was determined by Image-Pro Plus 6.0 software based on the OM images, and the measurement error was about 0.5%. The tensile samples with gauge dimensions of 10×1×1 mm^3 (length × width × thickness) were prepared by the electric spark method. All tensile samples were ground and finally polished using a 1.0 μm diamond paste. The tensile tests were conducted in an Instron 5565 testing machine at room temperature, using a constant strain rate of 1×10^{-4} s^{-1}. Each experiment was repeated at least 3 times. The deformed samples were investigated by SEM to reveal the deformation and fracture features.

3. Results

Figure 1a demonstrates the typical patterns of sample S3. It exhibits a composite structure, consisting of the metallic glass matrix, the B2 phase of b**o**dy-centered cubic structure, and the B19' phase of monoclinic structure. Similar results were also found in samples S1 and S2 (not shown here). The inset in Fig. 1a shows an optical metallograph of the microstructure of sample S3. The round and dark particles are B2 crystals, which are homogeneously distributed in the amorphous MG matrix. The average chemical compositions for the B2 phase and the amorphous MG matrix were detected by energy-dispersive spectroscopy (EDS) as $\underline{Zr_{50.9}Cu_{43.7}Al_{4.1}Nb_{1.3}}$ and $Zr_{49.6}Cu_{44.3}Al_{3.6}Nb_{2.5}$, respectively. It is clear that the difference between the chemical compositions of the B2 phase and the amorphous MG matrix is very small, which indicates that the precipitation of the B2 phase from the melt

during solidification does not involve strong element diffusion. Figure 1b shows that the volume fractions of the B2 phase are 9.9%, 18.2%, and 45.1% for samples S1, S2, and S3, respectively.

Figure 2a shows the tensile engineering stress-strain curves of S1, S2, and S3 with different crystalline volume fractions. When the B2 phase was introduced, a significantly continuous transformation from unstable to stable tensile plastic deformation was found in the MGC with various crystalline volume fractions. For S1 with a B2 volume fraction of 9.9%, it failed quickly once yielding began, and there was only 1.6±0.5% plastic strain before fracture, showing a typical brittle fracture at a strength of 1718±25 MPa. As far as S2 was concerned, a remarkable unstable tensile plastic strain of 5.6±0.5% occurred before fracture. However, the plastic deformation was characterized with obvious work softening once the yield began at a stress of 1688±25 MPa. A typical flow serration was found in the plastic region of S2 (see details in Fig. 2b), which is usually found in the compressive plastic deformation of some ductile monolithic MGs. As the volume fraction of the B2 phase increased to 45.1%, the tensile plastic deformation stability was remarkably improved, as seen for S3 in Fig. 2a. The total strain before necking and fracture was 19.2% for S3. As to S3, with a crystalline volume fraction of 45.1%, it firstly yielded at 566 MPa and then secondly at 1200 MPa. This first and second yielding is induced by the martensitic transformation of the B2 phase and the initiation of the shear bands in the glassy matrix, respectively [21,24]. Its flow serration was significantly smaller than that of S2, as shown in Fig. 2b. Figure 2c shows the true stress-strain curve and the corresponding work-hardening rate for S3 subjected to uniaxial tension. It is clear that S3 underwent significant work hardening to the stress of 1843 MPa, which is almost 60% higher than the yield stress of 1200 MPa. The average strain-hardening rate ($\theta = \frac{d\sigma}{d\varepsilon}$) for S3 was 3580 MPa, and the normalized strain-hardening rate ($K = \frac{\theta}{\sigma_S}$) was about 2.98.

Figure 2d shows the deformation feature of S3. The plastic deformation was very uniform in the whole gauge region. No long penetrating shear bands can be observed in the

whole deformation region. High density shear bands were formed near the B2/MG interface, and also severe plastic deformation occurred inside the B2 phases (Fig. 2e). Obvious B19' deformation twins and the interaction between the twins were found in the B2 phase region (see inset in Fig. 2e), which was also found in the $Zr_{46.25}Cu_{44.25}Al_{7.5}Er_2$ MGC [26], CuZr alloy [27], and the $Zr_{48}Cu_{47.5}Al_4Co_{0.5}$ MGC [21]. For the as-cast S3, there were two major phases: the metallic glass matrix and the B2 phase with a body-centred cubic (*bcc*) structure. However, when the sample was subjected to tensile deformation, the B2 peak significantly decreased. An obvious martensitic transformation also occurred, related to the process of a new monoclinic phase B19' formation in the B2 matrix (see Fig. 2f).

4. Discussion

The experimental results above clearly demonstrate that the stability of the tensile plastic deformation of ZrCu-based MGCs is greatly improved by the metastable B2 phase. It is believed that the stabilized tensile plastic deformation is attributed to the high work-hardening rate of the metastable B2 phase [21-23,25]. It was found that both primary and secondary twins are produced during the plastic deformation [27]. First, the primary twins formed on the sample at a relatively low tensile stress, and with the plastic deformation accumulating, secondary twins were formed (see the inset in Fig. 2(e)). The interaction of the primary and secondary twins results in the high work-hardening rate of the B2 phase [25]. In this condition, more interfaces between the B2 matrix and the martensite with deformation twins reduce the mean free path of the dislocations and accordingly improve the dynamic Hall-Petch effect of the *B2* phase. At the same time, more stress concentration sites form in the *B2*/MG interface [25].

In ZrCu-based MGCs, the maximum elastic strain of the MG matrix is about 2%, whereas the maximum elastic strain of the B2 phase is much smaller than 1% [25]. Therefore, when subjected to tensile loading, the B2 phase will firstly deform plastically. Its deformation is confined by the interface, and there is a large stress concentration at the interface. With the loading further increased, when the total strain of the *B2* is near 2%, the MG matrix will start

to deform plastically by forming shear bands, and the stress concentration sites near the interfaces facilitate the initiation of shear bands. Such phenomenon has also been analyzed for MG/crystalline multilayer composites [25,28,29]. Figure 2e is a typical SEM image showing that the shear bands initiate at the interface in S3. Therefore, it is considered that B2 particles can promote the formation of multiple shear bands, and the multiple shear bands will interact with those initiating from neighbouring B2 particles, leading to the large plastic strain in the ZrCu-based MGCs [25].

The flow serration in the stress-strain curves reflects the shear band behavior in MGs, and is related to the activation of the shear transformation zones and their dynamics [25,30]. As shown in Fig. 2b, the stress drop amplitude $\Delta\sigma$ is about 3.5±0.5 MPa for S2, and only 1.3±0.2 MPa for S3. The stress-strain curves indicate that S2 shows chaotic plastic deformation behavior characterized by a Gaussian distribution of the shear avalanches, but S3 is more self-organized, and is represented by a power-law distribution of the shear avalanches [30]. This great change is induced by the microstructural heterogeneities of the *B2* phases. As is well known, an MG can store large elastic energy due to its high strength and large elastic deformation [31,32]. Once the shear band is initiated, the energy will be dissipated quickly in the propagating shear band. In the case of the *B2* reinforced MGC, the *B2* phase undergoes prevailing martensitic transformation long before the formation of shear bands, especially with the large volume fraction of the *B2* phase [25]. The martensitic transformation can dissipate most elastic energy, and decrease the elastic energy dissipated by the propagation of the shear band, which is reflected by the low stress drop of the stress-strain curve (see Fig. 2b) and the tiny and short shear bands in S3 (see Fig. 2d and 2e).

In MGCs, the tensile plastic deformation stability is very sensitive to the morphology of the shear bands [25]. For an MGC manifesting stable tensile plastic deformation behavior, at least two conditions should be satisfied: one is that the length (free path) of the shear band should be short enough or lower than a critical value [32], and another requires effective interaction between the shear bands [25]. For the present MGC sample, S3, the volume fraction of the B2 phase is high enough to shorten the free path to under the critical value.

Meanwhile, the martensitic transformation can produce sufficient stress concentration sites exciting the high dense shear bands from different directions. A short free path of the shear band as well as high density shear bands can significantly reduce the elastic energy density dissipation on the shear band, and the multi-direction enhances the interaction of the shear bands, thus the propagation of shear band is stabilized and the formation of cracks in the shear band is delayed [25,33]. Furthermore, the martensitic transformation of the B2 phase and the subsequent dislocation glide can relieve the stress concentration near the interface between the MG and the B2 phases, which delays the formation of cracks at the interface [25]. Therefore, the ZrCu-based MGC-III can promote the formation and interaction of multiple shear bands and show excellent tensile plastic deformation behavior.

To achieve homogeneous plastic deformation in MGCs, besides the formation and interaction of multiple shear bands, there should be a match of the strain-hardening rates between the ductile phase and the MG matrix. As pointed out previously, the initial homogeneous plastic deformation of MGC is related to its normalized strain-hardening rate [34], which is

$$K = \frac{1}{\sigma_0}\frac{d\sigma}{d\varepsilon}. \quad (1)$$

Here, K is the normalized strain-hardening rate of the MGC, σ_0 is the yield strength of the MGC, and $\frac{d\sigma}{d\varepsilon}$ is the strain-hardening rate of the MGC. For a simplistic analysis, it is supposed that the MG matrix and the ductile phase yield synchronically (Actually, the ductile phase yields before the MG matrix). Taking $\sigma = f_{\mathrm{P}}\sigma_{\mathrm{P}} + f_{\mathrm{M}}\sigma_{\mathrm{M}}$ (f_{P} and f_{M} are the volume fractions for the ductile phase and the MG matrix; σ_{P} and σ_{M} are the stresses for the ductile phase and the MG matrix, respectively) and $\sigma_0 = f_{\mathrm{P}}\sigma_0^{\mathrm{P}} + f_{\mathrm{M}}\sigma_0^{\mathrm{M}}$ (σ_0^{P} and σ_0^{M} are the yield strengths of the ductile phase and the MG matrix, respectively) into Eq. 1, one gets

$$K = \frac{f_{\mathrm{P}} \dfrac{d\sigma_{\mathrm{P}}}{d\varepsilon} + f_{\mathrm{M}} \dfrac{d\sigma_{\mathrm{M}}}{d\varepsilon}}{f_{\mathrm{P}}\sigma_0^{\mathrm{P}} + f_{\mathrm{M}}\sigma_0^{\mathrm{M}}}. \quad (2)$$

Eq. 3 also can be written as

$$K = \frac{f_{\mathrm{P}}\sigma_0^{\mathrm{P}}K_{\mathrm{P}} + f_{\mathrm{M}}\sigma_0^{\mathrm{M}}K_{\mathrm{M}}}{f_{\mathrm{P}}\sigma_0^{\mathrm{P}} + f_{\mathrm{M}}\sigma_0^{\mathrm{M}}}. \quad (3)$$

Here, $K_{\mathrm{P}} = \frac{1}{\sigma_0^{\mathrm{P}}}\frac{d\sigma_{\mathrm{P}}}{d\varepsilon}$ and $K_{\mathrm{M}} = \frac{1}{\sigma_0^{\mathrm{M}}}\frac{d\sigma_{\mathrm{M}}}{d\varepsilon}$ are the normalized strain-hardening rates for the ductile phase and the MGC, respectively. Since $f_{\mathrm{M}} = 1 - f_{\mathrm{P}}$ and the yield strength ratio $\alpha = \frac{\sigma_0^{\mathrm{M}}}{\sigma_0^{\mathrm{P}}}$, Eq. 3 becomes

$$K = \frac{f_{\mathrm{P}}}{f_{\mathrm{P}} + (1 - f_{\mathrm{P}})\alpha}K_{\mathrm{P}} + \frac{(1 - f_{\mathrm{P}})\alpha}{f_{\mathrm{P}} + (1 - f_{\mathrm{P}})\alpha}K_{\mathrm{M}}. \quad (4)$$

This is the equation of the normalized strain-hardening rate for an MGC. As reported in literature [34], if $K \geq 1$, stable plastic deformation can occur in MGC/PT bimetals, otherwise instable plastic deformation occurs. Therefore, by substituting K_{P}=17.4 (typical for B2 phase [34]), K_{M}=0 [34], and α=3.53 in Eq. 4, we can obtain K as a function of the volume fraction f_{P} of the ductile phase, as shown in Fig. 3a. It can be seen that the normalized strain-hardening rate of the MGC monotonically increases with the volume fraction f_{P} of the ductile phase. When the volume fraction f_{P} of the ductile phase is larger than 0.20, K is larger than 1, which is the critical value for the stable plastic deformation of the MGC. Obviously, for the present MGCs, only the specimen with f_{P}=45.1% can meet this requirement. For the other specimens with f_{P}=9.9% and 18.2%, their normalized strain-hardening rates are smaller than 1, so their plastic deformation is unstable, as shown in Fig. 3a and Fig. 2a. However, the typical normalized strain-hardening rate of the β dendrite ($Ti_{65.4}Zr_{19.3}Mo_{9.7}Cu_{5.6}$) precipitated in the $Ti_{43}Zr_{27}Mo_5Cu_{10}Be_{15}$ MGC is only 2.42 [18,34],

which is far smaller than that of the B2-reinforced MGC. To achieve stable plastic deformation, the volume fraction of β dendrite should be larger than 70%, as shown in Fig. 3a. Figure 4b shows the normalized strain-hardening rate of some MGCs with different volume fraction of the ductile phases. It is obvious that most β-dendrite-reinforced MGCs stay under the line $K_0 = 1.0$, even if the volume fraction is close 70%. However, for all B2-reinforced MGCs, they stay above the line $K_0 = 1.0$. Even if the volume fraction is smaller than 50%, they can maintain large normalized strain-hardening rate, and display stable plastic deformation [21], as shown in Fig. 3b.

Therefore, by formation and interaction of multiple shear bands, the B2-reinforced MGC with large normalized strain-hardening rate can undergo large stable plastic deformation. Figure 4 shows the tensile fracture strength-plastic strain data from previously reported Cu-, Zr-, and Ti-based MGCs and the present B2-MGC. For the previous reported β-MGCs and B2-MGCs [16,17,19,20,35-40], most are located on the left bottom with 1300 MPa$\leq \sigma_f \leq$ 1750 MPa and $\varepsilon_p \leq 4.0\%$. Only a few B2-MGCs [21] and metastable β-MGCs [20,39] show a mixture of large fracture strength ($\sigma_f \geq 1650$ MPa) and large plastic strain ($\varepsilon_p > 4.0\%$). As to the present B2-MGC, they are shown on the upper right corner of Fig. 4, with σ_f larger than 1800 MPa and ε_p larger than 14%, exhibiting a good combination of high fracture strength and large plastic strain. It's clear that by controlling the distribution of the B2 phase, the B2-MGC can achieve excellent mechanical performance.

5. Conclusions

In summary, this study indicates that the metastable B2 phase can effectively promote multiple shear bands and thus significantly improve the plastic deformation capability of B2-MGCs. The uniform plastic deformation of the ZrCu-based MGC originates from a deformation mechanism of the effective excitation of the stress concentration sites along the *B2*/MG interfaces. The effect of the ductile phase on the plastic stability of MGCs was also analyzed from the concept of the normalized strain-hardening rate. The critical volume

fractions for stable plastic deformation of B2- or β-reinforced MGCs were also calculated. This finding implies that the mechanical properties of MGC can be well tailored by choosing a suitable reinforcer and controlling its volume fraction.

Acknowledgements

The work was supported by the Research Grants Council of the Hong Kong Special Administrative Region, China (Project No. PolyU 511211), Liaoning BaiQianWan Talents Program (Grant No. 2014921056), and the Program for Liaoning Excellent Talents in University (Grant No. LJQ2014064).

References

[1] C.A. Schuh, T.C. Hufnagel, U. Ramamurty, Acta Mater., 55 (2007) 4067-4109.

[2] Z.F. Zhang, F.F. Wu, G. He, J. Eckert, J. Mater. Sci. Technol., 23 (2007) 747-767.

[3] J.R. Greer, J.T.M. De Hosson, Prog. Mater Sci., 56 (2011) 654-724.

[4] H. Chen, Y. He, G.J. Shiflet, S.J. Poon, Nature, 367 (1994) 541-543.

[5] F.F. Wu, Z.F. Zhang, F. Jiang, J. Sun, J. Shen, S.X. Mao, Appl. Phys. Lett., 90 (2007) 191909.

[6] F.F. Wu, W. Zheng, S.D. Wu, Z.F. Zhang, J. Shen, Acta Mater., 60 (2012) 2073-2081.

[7] C.A. Volkert, A. Donohue, F. Spaepen, J. Appl. Phys., 103 (2008) 083539.

[8] B.E. Schuster, Q. Wei, M.H. Ervin, S.O. Hruszkewycz, M.K. Miller, T.C. Hufnagel, K.T. Ramesh, Scripta Mater., 57 (2007) 517-520.

[9] H. Guo, P.F. Yan, Y.B. Wang, J. Tan, Z.F. Zhang, M.L. Sui, E. Ma, Nature Mater., 6 (2007) 735-739.

[10] D. Jang, J.R. Greer, Nature Mater., 9 (2010) 215-219.

[11] H. Kato, T. Hirano, A. Matsuo, Y. Kawamura, A. Inoue, Scripta Mater., 43 (2000) 503-507.

[12] A. Inoue, W. Zhang, T. Tsurui, A.R. Yavari, A.L. Greer, Philos. Mag. Lett., 85 (2005) 221-229.

[13] C. Fan, D.V. Louzguine, C.F. Li, A. Inoue, Appl. Phys. Lett., 75 (1999) 340-342.

[14] D.V. Louzguine, H. Kato, A. Inoue, Appl. Phys. Lett., 84 (2004) 1088-1089.

[15] C.C. Hays, C.P. Kim, W.L. Johnson, Phys. Rev. Lett., 84 (2000) 2901-2904.

[16] D.C. Hofmann, J.Y. Suh, A. Wiest, G. Duan, M.L. Lind, M.D. Demetriou, W.L. Johnson, Nature, 451 (2008) 1085-1090.

[17] D.C. Hofmann, J.Y. Suh, A. Wiest, M.L. Lind, M.D. Demetriou, W.L. Johnson, PNAS, 105 (2008) 20136.

[18] F.F. Wu, K.C. Chan, S.T. Li, G. Wang, P. Lin, Philos. Mag. Lett., 94 (2014) 233-241.

[19] F.F. Wu, Z.F. Zhang, A. Peker, S.X. Mao, J. Eckert, Phys. Rev. B, 75 (2007) 134201.

[20] Y.S. Oh, C.P. Kim, S. Lee, N.J. Kim, Acta Mater., 59 (2011) 7277-7286.

[21] Y. Wu, X.H. Xiao, G.L. Chen, C.T. Liu, Z.P. Lu, Adv. Mater., 22 (2010) 2770-2773.

[22] K.K. Song, S. Pauly, Y. Zhang, R. Li, S. Gorantla, N. Narayanan, U. Kühn, T. Gemming, J. Eckert, Acta Mater., 60 (2012) 6000-6012.

[23] S. Pauly, G. Liu, G. Wang, U. Kühn, N. Matterna, J. Eckert, Acta Mater., 57 (2009) 5445-5453.

[24] F.F. Wu, K.C. Chan, S.S. Jiang, S.H. Chen, G. Wang, Sci. Rep., 4 (2014) 5302.

[25] F.F. Wu, K.C. Chan, S.T. Li, G. Wang, J. Mater. Sci., 49 (2014) 2164-2170.

[26] K.K. Song, S. Pauly, B.A. Sun, Y. Zhang, J. Tan, U. Kühn, M. Stoica, J. Eckert, Intermetallics, 30 (2012) 132-138.

[27] J.W. Seo, D. Schryvers, Acta Mater., 46 (1998) 1165-1175.

[28] A. Donohue, F. Spaepen, R.G. Hoagland, A. Misra, Appl. Phys. Lett., 91 (2007) 241905.

[29] Y.M. Wang, J. Li, A.V. Hamza, T.W. Barbee, PNAS, 104 (2007) 11155-11160.

[30] G. Wang, K.C. Chan, L. Xia, P. Yu, J. Shen, W.H. Wang, Acta Mater., 57 (2009) 6146–6155.

[31] S.H. Chen, K.C. Chan, F.F. Wu, L. Xia, Appl. Phys. Lett., 104 (2014) 111907.

[32] F.F. Wu, Z.F. Zhang, S.X. Mao, Philos. Mag. Lett., 89 (2009) 178-184.

[33] F.F. Wu, W. Zheng, S.D. Wu, Z.F. Zhang, J. Shen, Int. J. Plast., 27 (2011) 560-575.

[34] F.F. Wu, S.T. Li, G.A. Zhang, X.F. Wu, P. Lin, Appl. Phys. Lett., 103 (2013) 151910.

[35] F. Szuecs, C.P. Kim, W.L. Johnson, Acta Mater., 49 (2001) 1507-1513.

[36] C. Jeon, C.P. Kim, S.H. Joo, H.S. Kim, S. Lee, Acta Mater., 61 (2013) 3012-3026.

[37] J.W. Qiao, A.C. Sun, E.W. Huang, Y. Zhang, P.K. Liaw, C.P. Chuang, Acta Mater., 59 (2011) 4126-4137.

[38] F.F. Wu, Z.F. Zhang, A. Peker, S.X. Mao, J. Das, J. Eckert, J. Mater. Res., 21 (2006) 2331-2336.

[39] C.P. Kim, Y.S. Oh, S. Lee, N.J. Kim, Scripta Mater., 65 (2011) 304-307.

[40] Y. Wu, H. Wang, H.H. Wu, Z.Y. Zhang, X.D. Hui, G.L. Chen, D. Ma, X.L. Wang, Z.P. Lu, Acta Mater., 59 (2011) 2928-2936.

Figures Caption

Fig. 1. (a) XRD pattern of metallic glass composite S3. The inset is the optical micrograph image of sample S3. (b) The volume fraction of B2 phase for S1, S2, and S3.

Fig. 2. (a) Tensile engineering stress-strain curves for the metallic glass composite samples S1, S2, and S3, respectively. (b) Enlarged stress-strain curves for showing the flow serrations of samples S2 and S3. (c) Tensile true stress-strain curve and the corresponding work-hardening rate for S3. (d) Macroscopic and (e) enlarged SEM images showing the tensile deformation features of S3. The inset in Fig. 2(e) is an enlarged image indicating the interaction between the twins. (f) XRD patterns showing the phase structure of S3 before and after deformation, as denoted as-cast and deformed, respectively. For the as-cast S3, there are two phases: the metallic glass matrix and the *B2* phase with a body-centred cubic (*bcc*) structure. For the deformed S3, there are three phases: the metallic glass matrix, *B2* phase, and *B19'* with monoclinic structure.

Fig. 3. (a) The calculated normalized strain-hardening rate for B2-MGCs and β-MGCs with different volume fraction of the ductile phase based on Eq. 4. (b) The normalized strain-hardening rate for B2-MGCs and β-MGCs [16,17,19-21,35-39]. The line $K_0 = 1.0$ is the reference line for homogeneous plastic deformation.

Fig. 4. Strength-ductility diagram of metallic glass composites [16,17,19-21,35-40].

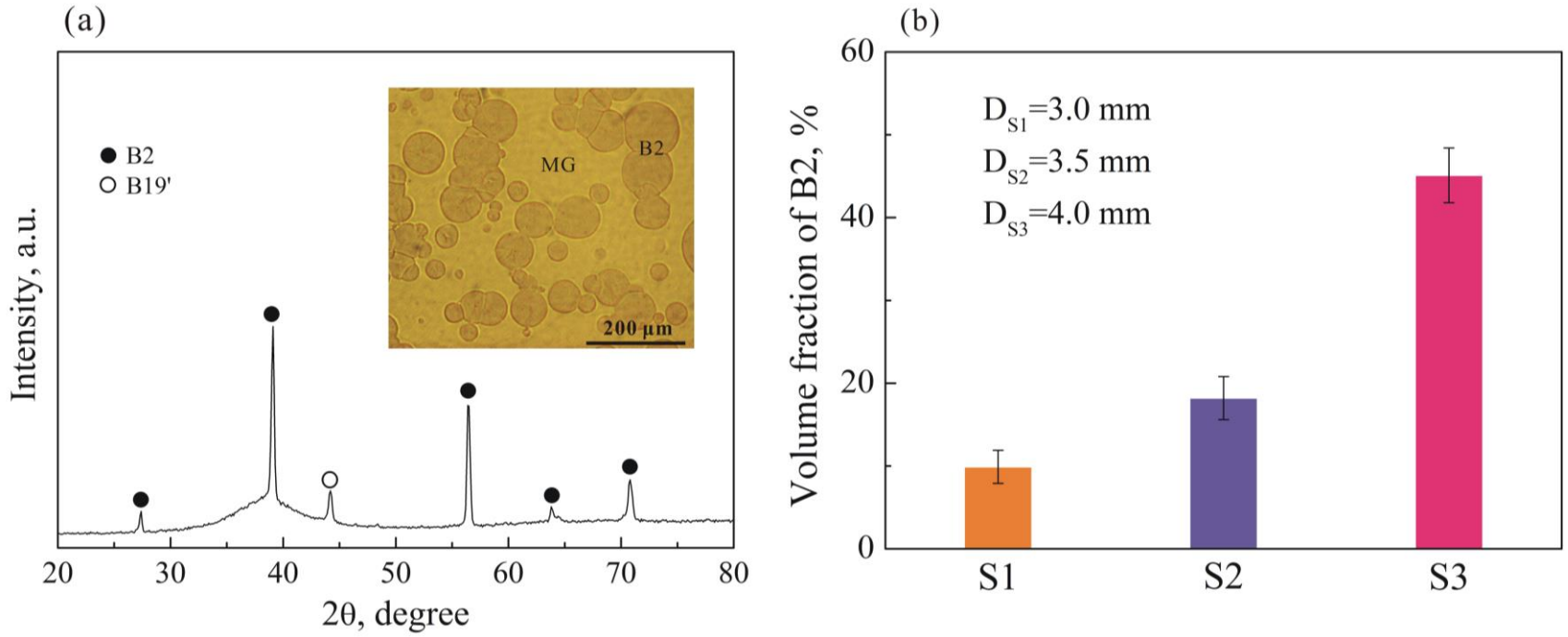
(a)
B2
B19'
MG
B2
200 µm
Intensity, a.u.
20
30
40
50
60
70
80
2θ, degree
(b)
60
40
20
0
Volume fraction of B2, %
D_S1=3.0 mm
D_S2=3.5 mm
D_S3=4.0 mm
S1
S2
S3

Fig. 1

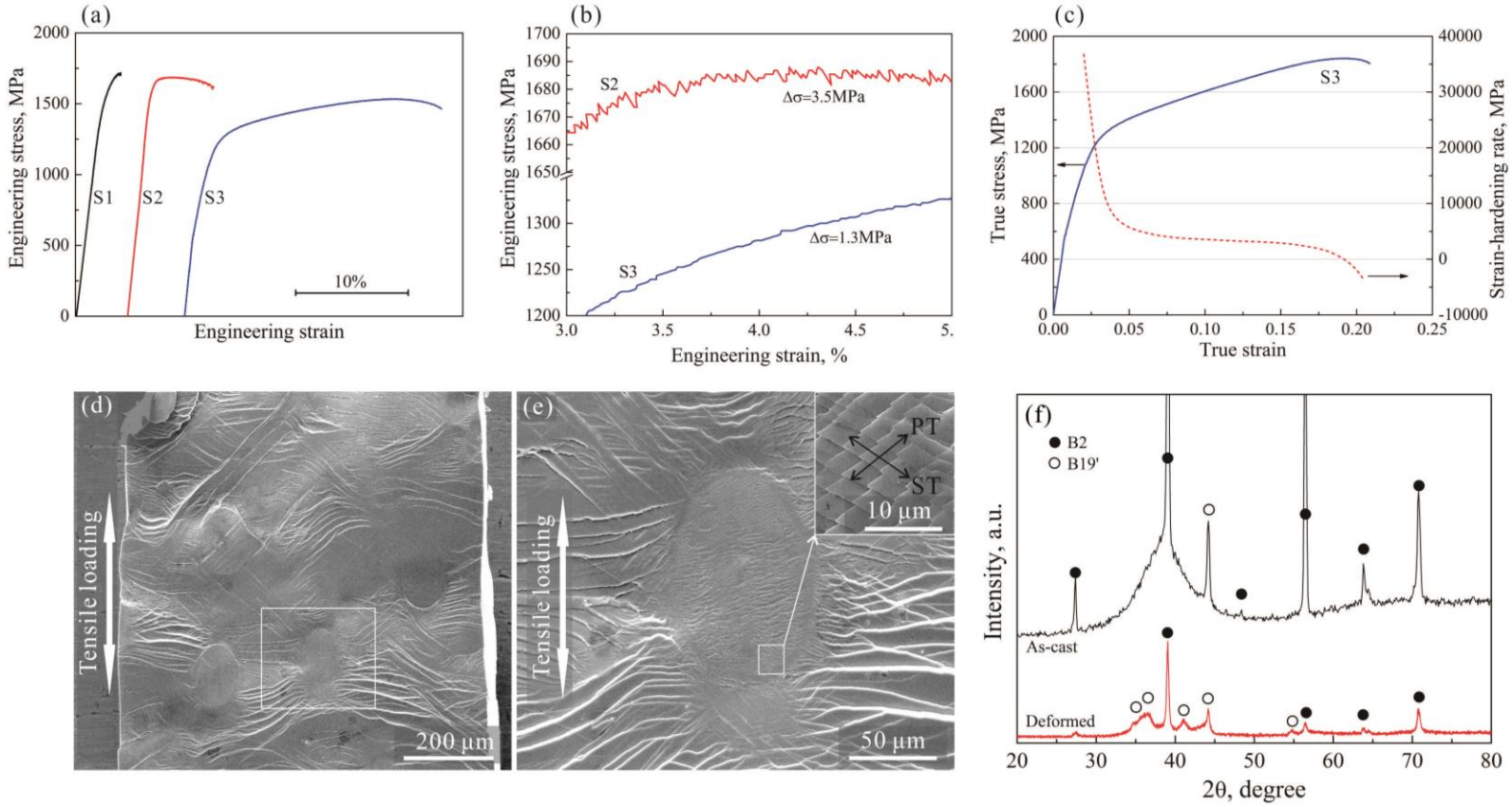
(a)
Engineering stress, MPa
Engineering strain
S1
S2
S3
10%
(b)
Engineering stress, MPa
Engineering strain, %
S2
Δσ=3.5MPa
S3
Δσ=1.3MPa
(c)
True stress, MPa
Strain-hardening rate, MPa
True strain
S3
(d)
Tensile loading
200 μm
(e)
Tensile loading
PT
ST
10 μm
50 μm
(f)
B2
B19'
Intensity, a.u.
As-cast
Deformed
2θ, degree

Fig. 2

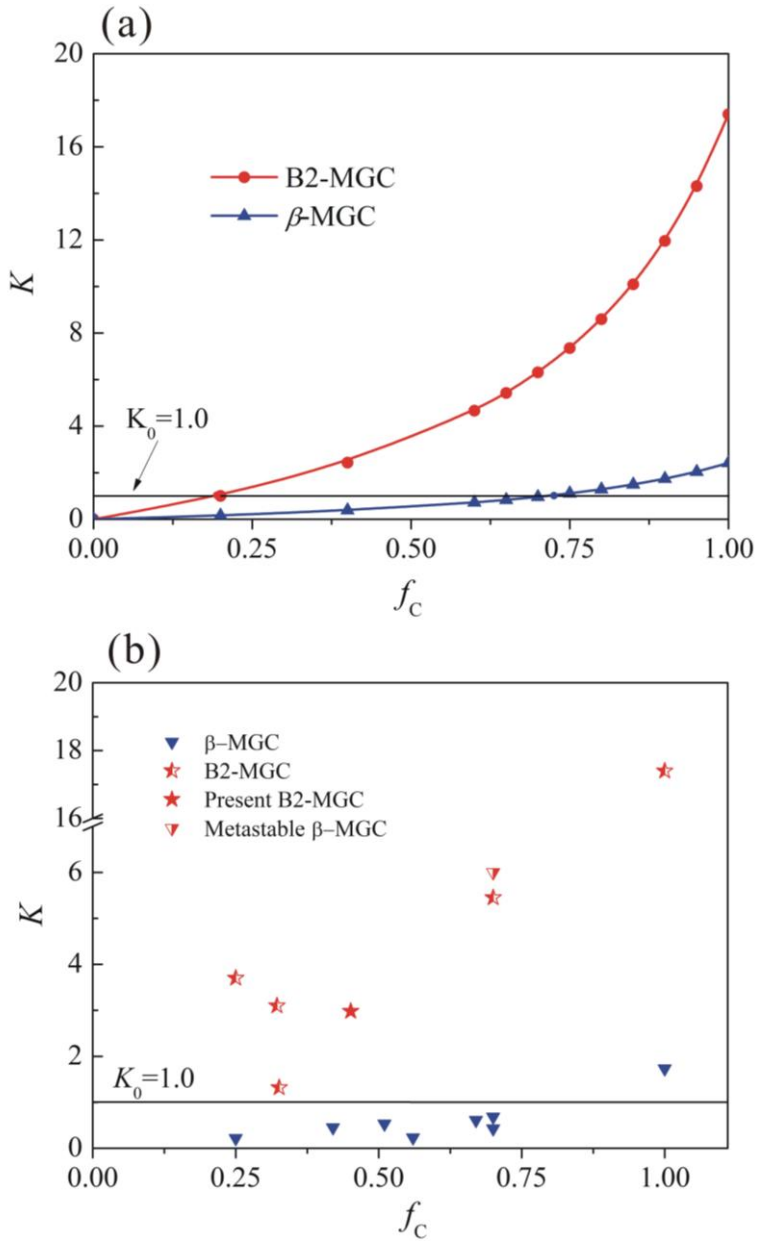
(a)
B2-MGC
β-MGC
K
K0=1.0
fC
(b)
β–MGC
B2-MGC
Present B2-MGC
Metastable β–MGC
K
K0=1.0
fC

Fig. 3

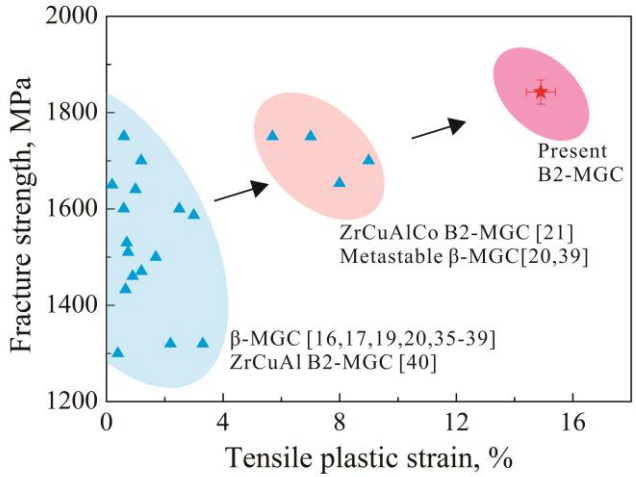
2000
1800
1600
1400
1200
Fracture strength, MPa
0
4
8
12
16
Tensile plastic strain, %
Present
B2-MGC
ZrCuAlCo B2-MGC [21]
Metastable β-MGC[20,39]
β-MGC [16,17,19,20,35-39]
ZrCuAl B2-MGC [40]

Fig. 4